ACS SENSORS

pubs.acs.org/acssensors Article

Photoexcited NO_2 Enables Accelerated Response and Recovery Kinetics in Light-Activated NO_2 Gas Sensing

Xin Geng,[⊥] Xiaolong Liu,[⊥] Lalani Mawella-Vithanage, Chathuranga C. Hewa-Rahinduwage, Liang Zhang, Stephanie L. Brock, Ting Tan,* and Long Luo*

Cite This: https://doi.org/10.1021/acssensors.1c01694 Read Online

ACCESS | Metrics & More | Article Recommendations | Supporting Information

ABSTRACT: Slow response and recovery kinetics is a major challenge for practical room-temperature NO_2 gas sensing. Here, we report the use of visible light illumination to significantly shorten the response and recovery times of a PbSe quantum dot (QD) gel sensor by 21% (to 27 s) and 63% (to 102 s), respectively. When combined with its high response (0.04%/ppb) and ultralow limit of detection (3 ppb), the reduction in response and recovery time makes the PbSe QD gel sensor among the best p-type room-temperature NO_2 sensors reported to date. A combined experimental and theoretical investigation reveals that the accelerated response and recovery time is primarily due to photoexcitation of NO_2 gaseous molecules and adsorbed NO_2 on the gel surface, rather than the excitation of the semiconductor sensing material, as suggested by the currently prevailing light-activated gas-sensing theory. Furthermore, we find that the extent of improvement attained in the recovery speed also depends on the distribution of excited electrons in the adsorbed NO_2/QD gel system. This work suggests that the design of light-activated sensor platforms may benefit from a careful assessment of the photophysics of the analyte in the gas phase and when adsorbed onto the semiconductor surface.

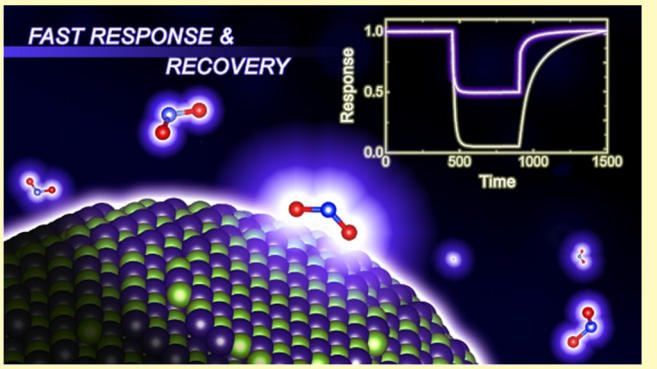

KEYWORDS: *NO_2 sensor, room-temperature gas sensing, light activation, quantum dot gel, quantum embedding method*

Atmospheric nitrogen dioxide (NO_2) has long been known to cause adverse effects on human health and the environment.[1−3] Most recently, a positive correlation between ppb-level NO_2 in urban air pollution and COVID-19 mortality rates was also found: an increase of 4.6 ppb in atmospheric NO_2 concentration is associated with a 16.2% increase of COVID-19 mortality rate in the United States.[4] The increasing public awareness of NO_2 pollution and its harmful effects have driven the development of NO_2 detection and remediation methods. Semiconductor NO_2 gas sensors are deemed a potential solution toward low-cost atmospheric NO_2 monitoring and thus have attracted significant attention from researchers.[5] Conventional semiconductor gas sensors typically operate at an elevated working temperature (100−500 °C) to achieve fast sensor response and recovery, which is crucial for air quality monitoring applications.[6−8] However, the high working temperature has several main drawbacks, including high power consumption (limiting its utility in portable devices), potential safety issues in the presence of explosive gases, and—for nanomaterial-based sensors in particular—poor long-term stability.[6] As a result, lowering the operating temperature, preferably to room temperature, is of significant interest for the development of practical NO_2 gas sensors.

For room-temperature NO_2 gas sensing, the slow response and recovery kinetics is a major hurdle.[9] Figure 1a summarizes the response and recovery times (t_{res} and t_{rec}) of 202 state-of-the-art room-temperature NO_2 gas sensors in the literature (Table S1). t_{res} and t_{rec} are defined as the times taken for the sensor response to vary by 90% during NO_2 exposure and removal, respectively. Note that for a fair comparison, we only considered the sensors that clearly reached a signal plateau when exposed to NO_2 and successfully returned to the baseline after NO_2 was removed. The statistics of t_{res} and t_{rec} show that approximately one-half of these sensors require a total response and recovery time (t_{res} + t_{rec}) > 1000 s, while only five have (t_{res} + t_{rec}) < 100 s. The room-temperature NO_2 gas sensors with the fastest response and recovery are the CdS and CdSe quantum dot (QD) gels (CdS: t_{res} = 28 s and t_{rec} = 29 s, orange circle in Figure 1a; CdSe: t_{res} = 24 s and t_{rec} = 31 s, red diamond in Figure 1a), previously developed by our group.[10]

Received: August 9, 2021
Accepted: November 1, 2021

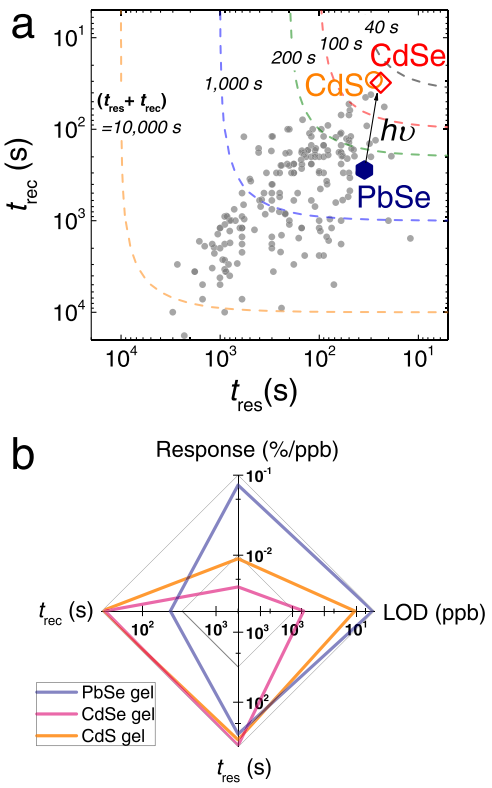

Figure 1. (a) Summary of the response time (t_{rec}) and recovery time (t_{res}) of 202 state-of-the-art room-temperature NO_2 gas sensors in the literature with the contour lines highlighting the different (t_{rec} + t_{res}) values. (b) Comparison between PbSe, CdSe, and CdS QD gel sensors (without light activation) in terms of t_{rec}, t_{res}, normalized sensor response (% electrical resistance change per ppb NO_2), and LOD.

The exceptional response and recovery kinetics of the QD gel sensors arises from their unique structure and surface chemistry. Specifically, the interconnected pore-matter architecture of the QD gel enables efficient gas exchange throughout the gel network, facilitating interactions between NO_2 and the QD gel surfaces, and thus, rapid response. Meanwhile, the relatively weak yet specific adsorption of NO_2 on the Cd sites of the CdS and CdSe gel surface ensures superior sensor selectivity toward NO_2 while enabling the quick release of the adsorbed NO_2 upon removal of NO_2 gas from the environment, resulting in fast recovery. However, the weak NO_2 adsorption on CdS and CdSe gels is a double-edged sword, as it correlates to a lower sensor response and limit of detection (LOD) when compared to other room-temperature p-type semiconductor NO_2 gas sensors (Table S2 and Figure 1b). Replacing weak-NO_2-binding Cd with strong-NO_2-binding Pb in the QD gel addresses the response and LOD limitations, achieving the best measured LOD of 3 ppb with a little negative impact on the response time (t_{res} = 35 s), but at a price of a 10-times slower recovery (t_{rec} = 279 s for PbSe vs 28 s for CdS and 24 s for CdSe, Figure 1b), sending us back to the drawing board.

Apart from heating and introducing weak-binding sites, light illumination is another possible strategy for shortening t_{rec}. Previous studies have found that light illumination can expedite both response and recovery of metal oxide gas sensors.[11] For example, Lu et al.[12] reported the t_{res} of their NO_2 sensor prepared from ZnO/SnO_2 nanocomposites to 200 ppb NO_2 was reduced from 12 min (without UV) to 7 min (with UV), and the recovery time was shortened from 14 min (without UV) to 8 min (with UV). This strategy has also proven effective for other semiconductors such as MoS_2,[13−17] $MoTe_2$,[18] SnS_2,[19,20] graphene,[21] and metal−organic frameworks[22] for NO_2 sensing. The current theory for explaining this light-activation phenomenon is that the photogenerated electron−hole pairs in the semiconductors react with the gas molecules to facilitate their chemisorption onto the sensor surface and desorption from the surface.[13,17,18,20,22−25]

Inspired by these prior findings, we sought to test the light-activation strategy on PbSe QD gel sensors, aiming to overcome the slow recovery without significantly compromising the other beneficial metrics. As control experiments, CdSe and CdS QD gels were also prepared, characterized, and tested for the effect of light illumination on their NO_2 sensing performance. These three QD gels with similar crystallite size and porosity but drastically different band gaps (PbSe: 1.45 eV, CdSe: 2.26 eV, and CdS: 2.55 eV) enabled us to determine whether the photoexcitation of the semiconductor sensing material is truly responsible for the improved response and recovery kinetics as suggested by the existing theory.

We found, surprisingly, that all three gels achieved the fastest response and recovery under violet light (395−400 nm) rather than at their corresponding excitation wavelengths. Notably, the t_{res} and t_{rec} of PbSe QD gel were shortened by 21% (to 27 s) and 63% (to 102 s), respectively, placing it in the top 10 sensors with respect to response/recovery speed, as shown in Figure 1a. When combined with its high response (0.04%/ppb) and ultralow LOD (3 ppb), the reduction in the response and recovery time makes the PbSe QD gel sensor among the best p-type room-temperature NO_2 sensors reported to date. In comparison, the improvement of t_{res} and t_{rec} was similar for the CdSe and CdS QD gels, both at ∼30%.

Our mechanistic study suggests that the excitation of NO_2 gas molecules and adsorbed NO_2 on QD gel should be the primary driver of the accelerated sensor response and recovery achieved under illumination conditions. The broad absorption characteristics of NO_2 between 250 and 650 nm enable the reduction of t_{res} for QD gels to be achieved across most of the UV−vis spectrum, but the most improvement is observed with violet light, which broadly corresponds to the peak absorption of NO_2 (403 nm). Theoretical calculations using embedded correlated wavefunction (ECW) theory,[26,27] which enables accurate assessment of both ground- and excited-state energies for gas adsorbates on a heterogeneous surface,[28−30] suggest that the maximum excitation of the adsorbed NO_2 occurs in the violet region as well, producing the most significant effects on NO_2 desorption. Finally, we show that the underlying mechanism accounting for the different levels of improvement of t_{rec} between PbSe and CdSe/S QD gels to be the different excited-state electron distributions in the QD gel-NO_2 systems.

RESULTS AND DISCUSSION

QD Gel Synthesis and Characterization. We carried out this study by first synthesizing structurally similar PbSe, CdSe, and CdS QD gels. CdSe and CdS QD gels were prepared by direct electrochemical gelation (or electrogelation) of nearly monodisperse spherical CdSe and CdS QDs (CdSe: 3.0 ± 0.3 nm and CdS: 3.2 ± 0.4 nm in diameter) following the previously reported procedures (Figure S1).[10] Briefly, we synthesized the CdSe and CdS QDs using a hot-injection method and performed ligand exchange with a short-chain

https://doi.org/10.1021/acssensors.1c01694
ACS Sens. XXXX, XXX, XXX−XXX

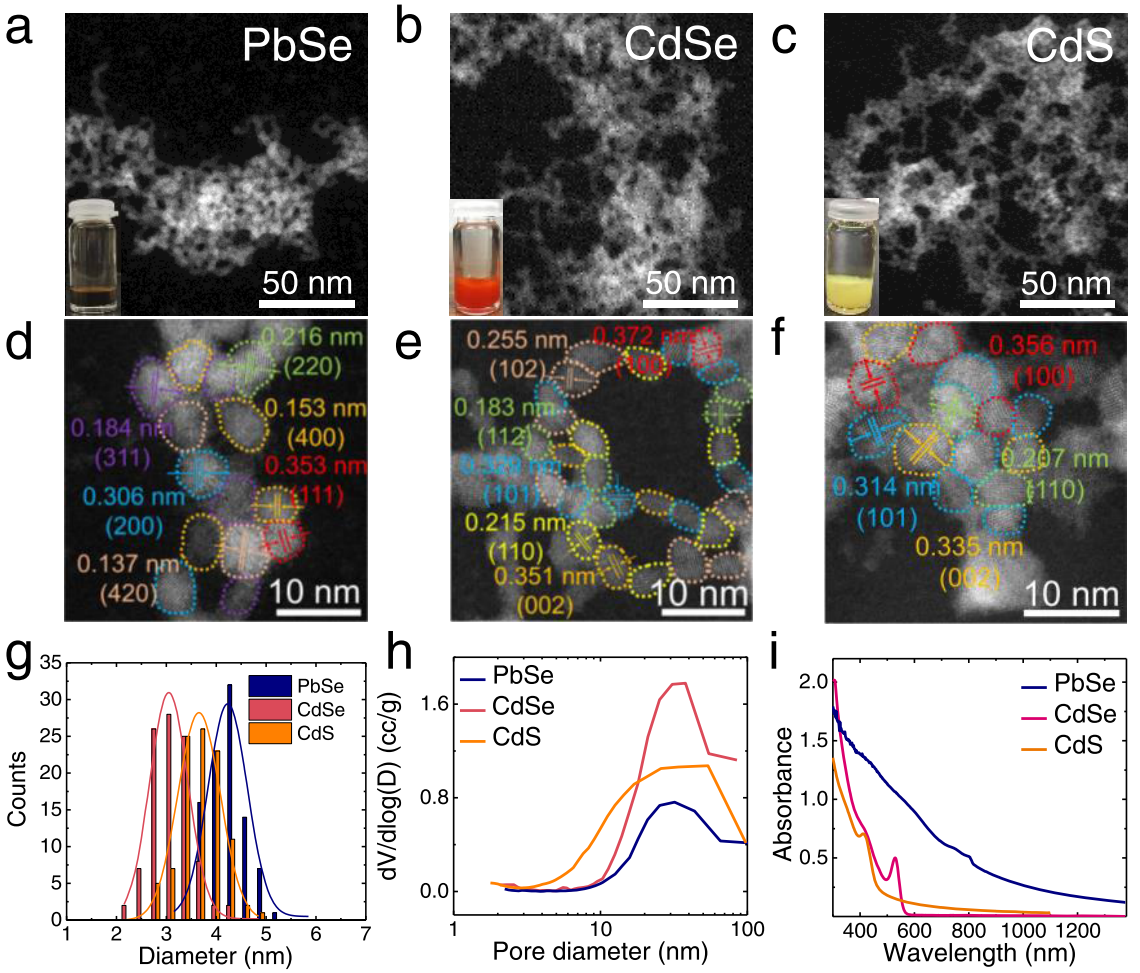

Figure 2. Structural characterization of CdSe, PbSe, and CdS QD gels. (a–c) Low-magnification STEM images of PbSe, CdSe, and CdS QD xerogels by drop-casting wet gels on TEM grids and drying in air. Inset: the corresponding photographs of their wet gels. (d–f), High-resolution STEM images of PbSe, CdSe, and CdS QD xerogels. The crystallites in the images are color-coded according to their lattice fringes: the (111), (200), (220), (311), (400), and (420) planes of cubic PbSe for PbSe QD gel; the (100), (002), (101), (102), (110), and (112) planes of hexagonal CdSe for CdSe QD gel; and the (100), (002), (101), and (110) planes of hexagonal CdS for CdS QD gel. (g) Size distribution histograms of the QD building blocks in PbSe, CdSe, and CdS QD gels. (h) Barrett–Joyner–Halenda pore size distribution plots. (i) Solution-phase UV–visible absorption spectra.

thiolate ligand, thioglycolic acid, before electrogelation.[31] Then, two Pt foils along with an Ag/AgCl/sat. KCl reference electrode were immersed in an electrolyte solution containing the thioglycolate-capped QDs. An electrode potential of 1.5 V was applied at the working electrode for 60 min to remove the thiolate ligands oxidatively (to disulfides) and further oxidize the QDs to form dichalcogenide bonds between them, producing a macroscale translucent wet gel (Figure 2b,c, insets). Under a scanning transmission electron microscope (STEM), CdSe and CdS QD wet gels show a mesoporous network with the pore size ranging from 2 to 50 nm (Figure 2b,c). The QD building blocks of both gels were crystalline and randomly oriented, as evidenced by various lattice fringes attributed to multiple planes of hexagonal (wurtzite) CdSe and CdS (Figure 2e,f).

Because of the slow gelation kinetics of cubic polymorphs (i.e., PbSe) relative to hexagonal polymorphs (i.e., CdSe and CdS),[31,32] our strategy for targeting PbSe QD gels involves the initial synthesis of hexagonal CdSe QD gels followed by cation exchange of Cd^{2+} for Pb^{2+}. To minimize the structural disruption of the QD gel during cation exchange,[33] we used a low concentration (25 mM) of $Pb(NO_3)_2$ in methanol to slow down the ion exchange kinetics. After three days of cation exchange, the orange CdSe wet gel turned utterly black (Figure 2a, inset), indicating the formation of a PbSe QD gel. The lattice fringes assigned to the (111), (200), (220), (311), (400), and (420) planes of cubic PbSe in Figure 2d confirmed the complete exchange of Cd with Pb in the PbSe QD gel. Although the average size of QD building blocks in PbSe QD gel slightly increased to 4.2 ± 0.4 nm, it is still reasonably close to that of CdSe (3.0 ± 0.4 nm) and CdS (3.6 ± 0.4 nm) QD gels (Figure 2g). Powder X-ray diffraction (PXRD) was utilized to analyze the crystallinity of as-prepared PbSe, CdSe, and CdS QD gels (Figure S2). The characteristic peaks of cubic PbSe, hexagonal CdSe, and hexagonal CdS, are present in the corresponding gels. The crystallite sizes of PbSe, CdSe, and CdS gels were estimated to be 4.4 ± 0.3, 3.2 ± 0.2, and 3.7 ± 0.3 nm, respectively (Table S3), determined using a modification of the Scherrer equation,[34,35] in excellent agreement with the STEM results.

The porosity of PbSe, CdSe, and CdS QD gels was characterized by nitrogen physisorption. The wet gels were subjected to solvent exchange in acetone followed by supercritical CO_2 drying to produce aerogels before porosity

https://doi.org/10.1021/acssensors.1c01694
ACS Sens. XXXX, XXX, XXX–XXX

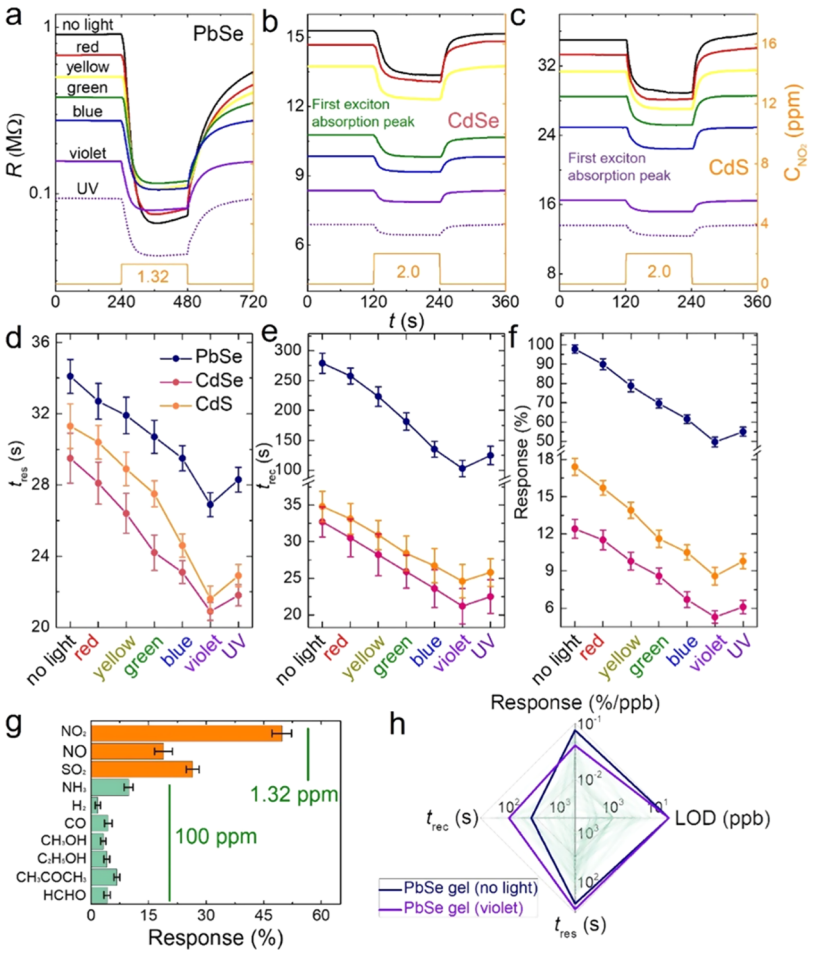

Figure 3. (a–c) Response–recovery curves of PbSe, CdSe, and CdS QD gel sensors toward NO_2 under 1.0 mW/cm^2 LED light illumination with different wavelengths at room temperature. C_{NO2} = 1.32 ppm for PbSe QD gel, and 2 ppm for CdSe and CdS QD gel. (d–f) t_{res}, t_{rec}, and the response of the PbSe, CdSe, and CdS QD gel sensors under different lights. The error bars represent the standard deviations of three response–recovery test results. (g) Responses of the PbSe QD gel sensor to different 100 ppm gases at room temperature (NO_2, NO, and SO_2 concentrations are 1.32 ppm). (h) Comparison between the PbSe QD gel sensor with (violet line) and without (blue line) violet-light illumination and 110 state-of-the-art room-temperature p-type NO_2 gas sensors in the literature (green lines) in terms of sensor response (%/ppb), LOD, t_{res}, and t_{rec}.

characterization. All three aerogels exhibited the characteristic type-IV isotherm for mesoporous materials (Figure S3). The surface areas of PbSe, CdSe, and CdS aerogels were estimated to be 90.9, 209.4, and 220.1 m^2/g, respectively, based on the Brunauer–Emmett–Teller (BET) model.[36] Their pore-size distributions are displayed in Figure 2h, obtained by fitting the desorption branch of the isotherm to the Barrett–Joyner–Halenda model.[37] The average pore diameters of PbSe, CdSe, and CdS gels were similar: 23.3, 22.3, and 20.5 nm, with cumulative pore volumes of 0.6, 1.3, and 1.2 cm^3/g, as listed in Table S4. Note that the smaller BET surface area and cumulative pore volume of the PbSe gel relative to CdSe and CdS gels is a function of the larger atomic mass of Pb relative to Cd. Thus, conversion to molar surface area yields values of 171 cm^3/mol (PbSe), 249 cm^3/mol (CdSe), and 174 cm^3/mol (CdS).

Figure 2i shows the UV–vis absorption spectra of CdSe, PbSe, and CdS QD wet gels. The first exciton absorption peaks of the CdSe and CdS QD gels are located at ~530 and ~412 nm, respectively, corresponding to green and violet light, while the PbSe gel absorbs over the entire UV–vis range, extending into the infrared region. The optical band gaps of PbSe, CdSe, and CdS gels are estimated to be 1.45, 2.26, and 2.55 eV based on Tauc plots (Figure S4).[38,39] These values exceed those of bulk PbSe (0.27 eV),[40] CdSe (1.7 eV), and CdS (2.42 eV),[41] suggesting that the quantum confinement characteristics of the QDs are retained in the gels despite being linked in a three-dimensional (3D) mesoporous framework.

NO_2 Gas-Sensing Performance. QD gel sensors were prepared by drop-casting 10 μL of PbSe, CdSe, or CdS wet gels on a sensor substrate patterned with interdigitated Pt electrodes and drying in air to form a xerogel sensing film. The film thickness was nearly identical: 3.6 μm (PbSe), 3.1 μm (CdSe), and 3.4 μm (CdS), respectively (Figure S5). All gas-sensing tests were carried out in a home-built Teflon chamber with light-emitting diode (LED) lamps placed in front of the sensing film at room temperature (Figure S6). The wavelength ranges of the red, yellow, green, blue, violet, and UV LED lights were 620–625, 570–575, 520–525, 460–465, 395–400, and 365–370 nm, respectively. The light intensity of all LED lamps is identical at 1.0 mW/cm^2 to avoid any effects arising from differences in light intensity. The sensor response was defined as $|R_a - R_g|/R_a$, where R_a and R_g are the equilibrium resistance after being exposed to air and NO_2 gas, respectively.

The typical response–recovery curves of PbSe, CdSe, and CdS QD gel sensors toward NO_2 under different LED lights

https://doi.org/10.1021/acssensors.1c01694
ACS Sens. XXXX, XXX, XXX–XXX

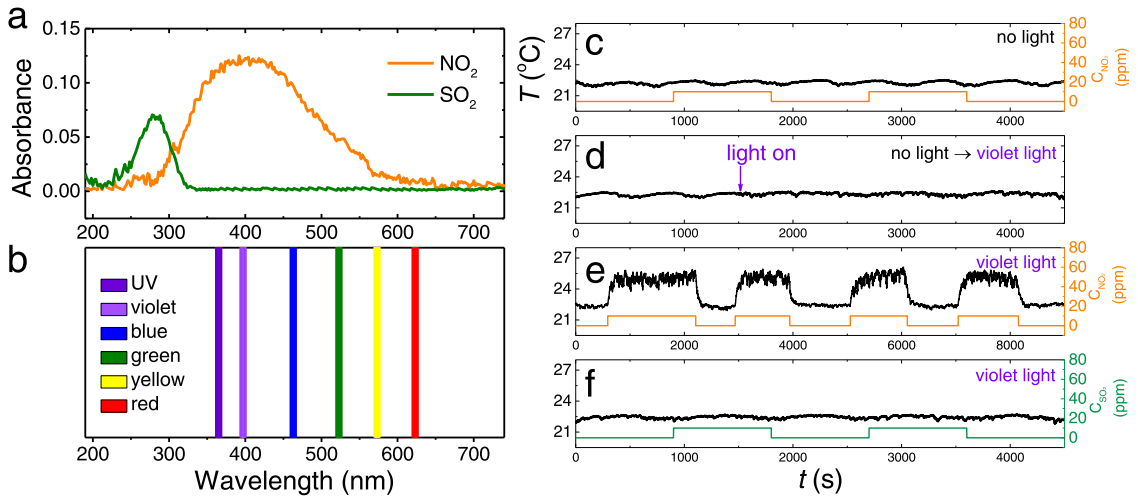

Figure 4. (a) UV−vis absorption spectrum of NO_2 and SO_2 gases. (b) Wavelength ranges of the LED lights used in this study. (c−f) Temperature inside the testing chamber vs time traces under no-light (c), during the no-light to violet-light transition (d), violet light with four pulses of 10 ppm NO_2 flow (e), and violet light with two pulses of 10 ppm SO_2 flow (f).

are shown in Figure 3a−c. All QD gels exhibited the characteristics of a p-type semiconductor gas sensor: the resistance (R) decreases upon exposure to NO_2 and returns to the baseline once NO_2 gas is removed. There are three apparent changes in these curves upon light illumination relative to the no-light conditions.

(i) The baseline resistance of the QD gels downshifted and continued dwindling as the light wavelength decreased, with the most significant drop taking place when the gel was photoexcited. For example, the CdSe QD gel shows the maximum baseline resistance change of 3 MΩ as the light was switched from lower-energy yellow (570−575 nm) to higher-energy green (520−525 nm) in Figure 3b because the green light exceeds the band gap of 2.26 eV (548 nm) and is close to the first exciton peak position. Such changes are expected because the photoexcitation of QD gels creates electron−hole pairs as additional charge carriers in the gel, reducing the electrical resistance.[42,43]

(ii) t_{res} and t_{rec} were shorter. For example, t_{res} and t_{rec} for the PbSe QD gel were 27 and 102 s under violet light, 21 and 63% less than their counterparts without light (Figure 3d,e).

(iii) The sensor response to NO_2 was lower, particularly for PbSe QD gel, which showed a response as high as 98% in the dark toward 1.32 ppm NO_2 but dropped to ∼50% under violet light (Figure 3f).

We further found that violet light is the most effective in accelerating the response and recovery of a QD gel sensor, regardless of the excitation wavelength of the gel. In addition, violet light is more effective in reducing t_{rec} of the PbSe QD gel than that of CdSe/S QD gels (63 vs 30%).

The reduced t_{res}, t_{rec}, and sensor response of PbSe QD gel sensors under light illumination were observed over a wide range of NO_2 concentrations from 3 ppb to 1.32 ppm (Figure S7). The linearity of the sensor response vs NO_2 concentration plot was not affected by the presence of light ($R^2 > 0.98$, Figure S8). The light-activated PbSe QD gel sensor was highly stable during multiple NO_2 exposure/removal cycles (Figure S9) and remained selective toward NO_2 (Figure 3g). The response of the violet-light-activated PbSe gel sensor to 1.32 ppm NO_2 is at least 1.9 times higher than other interfering gases, including 100 ppm electron-donating interfering gases (NH_3, H_2, CO, methanol, ethanol, acetone, and formaldehyde) and 1.32 ppm electron-accepting gases (NO and SO_2) at room temperature. Figure 3h compares the violet-light-activated PbSe gel sensor with 110 state-of-the-art p-type room-temperature NO_2 gas sensors in the literature in terms of sensor response (%/ppb), LOD, t_{res}, and t_{rec} (Table S2). Strikingly, the violet-light-activated PbSe gel sensor is among the best performers, with good sensor response (0.04%/ppb), ultralow LOD (3 ppb, the lowest experimentally measured LOD), and short t_{res} and t_{rec} (27 and 102 s, in the top 10 in terms of response/recovery speeds, Figure 1a). These data reveal that violet-light activation is a powerful strategy for improving the overall performance of PbSe QD gel sensors toward NO_2. However, humidity affects the sensing performance (Figure S10 and Table S5), leading to a reduced baseline resistance, response, and t_{rec} while increased t_{res} when humidity increases. It probably originates from the competitive adsorption between water and NO_2 molecules, decreasing the proportion of adsorption sites occupied by NO_2.

Light-Activated NO_2 Sensing Mechanism. According to the existing theory of light-activated gas sensing,[6] the photogenerated electron/hole pairs in the semiconductor are accountable for the reduced t_{res} and t_{rec}. When the sensor is exposed to NO_2, the excited electrons trap NO_2 gas molecules to facilitate the chemisorption of NO_2 onto the sensor surface and thus shorten t_{res}. Then, when NO_2 is removed from the system, the holes recombine with the trapped electrons in the adsorbed NO_2 resulting in its fast desorption. This theory emphasizes the role of photogenerated electron/hole pairs in facilitating adsorption/desorption of analytes and implies that a considerable reduction of t_{res} and t_{rec} should occur when the semiconductor sensor is photoexcited. However, our data does not conform to the theoretically predicted sensor behavior. For example, neither CdSe nor CdS show an abrupt change in t_{rec} upon illumination at the excitonic wavelength (Figure 3e). A small deviation for t_{res} is evident, but this change is less pronounced when compared to the change in t_{res} upon violet-light illumination (Figure 3d). Moreover, a dive into the literature on light-activated NO_2 sensing reveals that the best performance in terms of t_{res} and t_{rec} is achieved under blue or

https://doi.org/10.1021/acssensors.1c01694
ACS Sens. XXXX, XXX, XXX−XXX

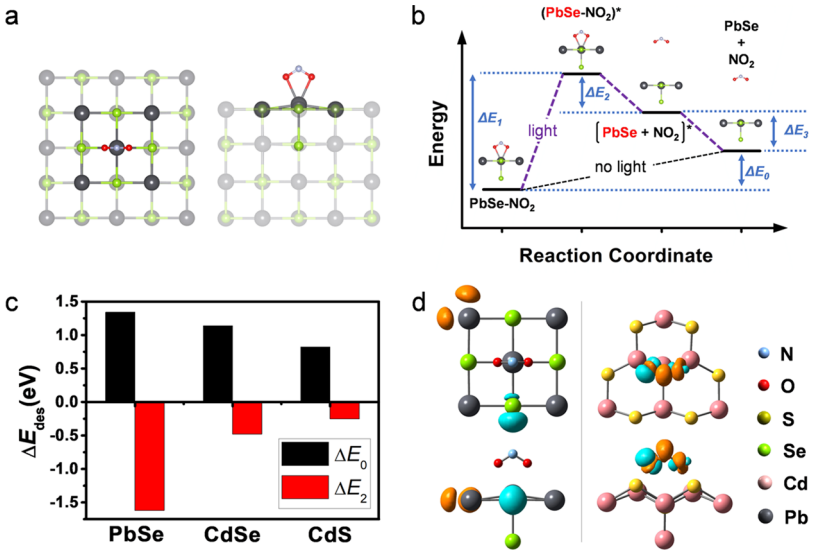

Figure 5. Theoretical calculation of NO_2 desorption from PbSe, CdSe, and CdS under no-light and light-illumination conditions. (a) Partition of the periodic PbSe-NO_2 system to an embedded region (i.e., a cluster of Pb_5Se_5 with $NO_{2,ads}$, the solid colored region) and its environment (i.e., the rest of the PbSe bulk, the faded colored region). (b) Schematic diagram of the energy profiles for NO_2 desorption from a PbSe(100) surface via a photoexcited state of $NO_{2,ads}$ ((PbSe-NO_2)*, purple dashed line) or via the ground state (black dashed line). (c) NO_2 desorption energies (ΔE_{des}) of PbSe, CdSe, and CdS at the ground state (black) and via the photoexcited state (red). (d) Electron density difference plots of PdSe-NO_2 and CdS-NO_2 systems, obtained by the excited-state electron density minus the corresponding ground-state one. The brown color represents an increase in density and the cyan color represents a decrease. The isosurface value is 0.004*e*.

violet light, and this is independent of the identity (i.e., band gap) of the semiconductor sensing platform.[44−47] The above data suggests that photoexcitation of a semiconductor sensor may not be responsible for the observed light-activated NO_2 sensing performance.

Taking one step back, we re-examined the classical theoretical model for the adsorption and desorption of NO_2 on a heterogeneous surface. NO_2 adsorption on a QD gel surface can be treated as a chemical reaction between NO_2 gaseous molecules ($NO_{2,gas}$) and the empty adsorption sites on the QD gel surface, yielding an adsorbed NO_2 molecule ($NO_{2,ads}$). The desorption process is simply the reverse reaction (eq 1).

$$NO_{2,gas} + \text{QD gel} \underset{k_{des}}{\overset{k_{ad}}{\rightleftharpoons}} NO_{2,ads} \quad (1)$$

The rate of adsorption, r_{ad}, and the rate of desorption, r_{des}, are given by

$$r_{ad} = k_{ad}P_{NO_2}[S] \text{ and } r_{des} = k_{des}[NO_{2,ads}]$$

where P_{NO_2} is the partial pressure of NO_2, [S] is the concentration of free binding sites on the QD gel surface, $[NO_{2,ads}]$ is the surface concentration of NO_2, and k_{ad} and k_{des} are constants of the forward adsorption reaction and backward desorption reaction in eq 1. The properties of all three substances in eq 1 should influence k_{ad} and k_{des}, but the existing theory for light-activated gas sensing narrowly focuses on the photoexcitation of QD gels but ignores the possible contributions from the other two (i.e., $NO_{2,gas}$ and $NO_{2,ads}$).

Photoexcitation of $NO_{2,gas}$. We note that $NO_{2,gas}$ has a broad absorption spectrum between 250 and 650 nm with a maximum near 403 nm (Figure 4a), covering the entire wavelength ranges of all of the light sources used in this study (Figure 4b). We confirmed the strong photoexcitation of $NO_{2,gas}$ under our experimental light illumination condition by unveiling the considerable photothermal effect due to the nonradiative relaxation of the electronically excited $NO_{2,gas}$ (denoted as $NO_{2,gas}$*) in the absence of the QD gel.[48] Figure 4e shows that the temperature inside the testing chamber increases by ∼3 °C when 10 ppm of NO_2 is illuminated by violet light (without QD gel). In contrast, there are no notable temperature changes when NO_2 is not illuminated (Figure 4c) or when the empty chamber is illuminated (Figure 4d). Note that $NO_{2,gas}$* is highly oxidizing (indeed, it reacts with H_2O to generate hydroxy radical),[49] so one can reasonably expect fast adsorption (i.e., short t_{res}) of $NO_{2,gas}$* onto a QD gel surface since the chemisorption of NO_2 also involves partial electron transfer from the QD gel to NO_2. More evidence supporting our claim that the photoexcitation of $NO_{2,gas}$ plays a vital role in light-activated NO_2 sensing can be seen in the similar trends for t_{res} and the photothermal effect (Figure S11), both of which peak under violet light.

Photoexcitation of $NO_{2,ads}$. Directly probing the excited state of $NO_{2,ads}$ on the QD gel surface is experimentally challenging due to the small number of $NO_{2,ads}$ molecules under typical gas-sensing conditions, so we turned to computational methods. Specifically, we employed ECW theory to accurately investigate both ground- and excited-state properties of $NO_{2,ads}$ on a QD gel surface. The ECW method partitions a target system into two subsystems (i.e., a small region of interest and its environment). The more efficient but less accurate method, density functional theory (DFT), was adopted to treat the environment and the interactions between the two subsystems, while highly accurate but expensive CW methods were applied to examine the small region of interest in the presence of the embedding potential. Taking $NO_{2,ads}$ on PbSe as an example, the region of interest is an embedded cluster of Pb_5Se_5 with one $NO_{2,ads}$ (the solid colored region in Figure 5a), and the environment is the rest of the PbSe bulk (the faded colored region in Figure 5a). The partitions of the CdS-NO_2 and CdSe-NO_2 systems are also

https://doi.org/10.1021/acssensors.1c01694
ACS Sens. XXXX, XXX, XXX−XXX

provided in Figure S12. In this work, we applied periodic DFT to study the environment and environment−cluster interactions, whereas the embedded complete active space second-order perturbation theory (emb-CASPT2)[50] was used to investigate the properties of the small cluster (see the experimental section and SI for details).

Figure 5b schematically shows the energy profiles for NO_2 desorption from a PbSe(100) surface via a photoexcited state of $NO_{2,ads}$ (denoted as (PbSe-NO_2)*, purple dashed line) or via the ground state (black dashed line). Both profiles start from $NO_{2,ads}$ on PbSe at the ground state (PbSe-NO_2). Without light, the desorption of NO_2 from PbSe requires overcoming the desorption energy, ΔE_0. Under light illumination with the appropriate excitation energy (ΔE_1), PbSe-NO_2 is promoted to (PbSe-NO_2)*, which later releases NO_2 and frees the adsorption site on PbSe at the desorption energy, ΔE_2. Note that the PbSe-NO_2 system at this point ([PbSe + NO_2]*) has not yet returned to the ground state even though NO_2 is no longer chemically bound to PbSe. The electron relaxation of [PbSe + NO_2]* to the ground states of NO_2 and PbSe releases additional energy, ΔE_3. Among all the energy terms, it is the desorption energies, ΔE_0 and ΔE_2, that dictate the desorption rate (manifested as t_{rec}) under no-light and light-illuminated conditions, respectively.

For NO_2 desorption at the ground state, PbSe shows the highest ΔE_0 of 1.34 eV, compared to 1.14 eV and 0.82 eV for CdSe and CdS (Figure 5c), in good agreement with the experimental observation that the PbSe QD gel sensor has the most sluggish recovery among the three (Figure 1a). For NO_2 desorption via the photoexcitation route, we found multiple excited states for $NO_{2,ads}$ on PbSe, CdSe, or CdS surfaces that occur in the visible light region (Figure S13). The excited state with the highest intensity, determined by the strongest oscillator strength in the ECW calculations, occurs at an excitation wavelength of 418 nm (2.97 eV), 387 nm (3.20 eV), and 456 nm (2.72 eV) for PbSe-NO_2, CdSe-NO_2, and CdS-NO_2, respectively. Thus, the maximum excitation of $NO_{2,ads}$ on the three QD gel surfaces occurs in the violet-light region (380−450 nm) or just outside it. Due to the elevated energy level of excited $NO_{2,ads}$, all ΔE_2 values are negative (Figure 5c), meaning NO_2 desorption under violet light is thermodynamically favorable, suggesting accelerated NO_2 desorption relative to the thermodynamically unfavorable no-light condition.

We also note that PbSe shows a larger difference between the two desorption energies ($|\Delta E_0 - \Delta E_2|$) than CdSe and CdS (Figure 5c), suggesting that violet light is more effective in shortening the t_{rec} of the PbSe QD gel relative to the CdSe/S QD gels, consistent with the experimental results in Figure 3e. To further identify the mechanistic origin of this difference, we analyzed the electron transition upon light excitation. Figure 5d shows the electron density difference plots for PbSe-NO_2 and CdS-NO_2, constructed by subtracting the ground-state electron density from the corresponding excited-state one. We found that the maximum excitation of PbSe-NO_2 involved an electron transition from Se to Pb, i.e., within PbSe. In contrast, the p $\rightarrow \pi^*$ transition of the NO_2 molecule is the major contributor to the maximum excitation of CdSe/S-NO_2 (Figures 5d and S14). These data suggest that the different levels of improvement of t_{rec} between PbSe and CdSe/S QD gels arise from the different spatial distributions of the excited-state electrons in the QD gel-NO_2 systems.

Based on the experimental and theoretical evidence discussed above, we conclude that the photoexcitation of $NO_{2,gas}$ and $NO_{2,ads}$ is more important than the photoexcitation of the QD gel itself for improving the response and recovery kinetics. $NO_{2,gas}$* is a strong oxidant, resulting in fast chemisorption kinetics and shorter t_{res}, while the photoexcitation of $NO_{2,ads}$ weakens the interactions between NO_2 and the QD gel, making NO_2 desorption highly thermodynamically favorable under light illumination, enhancing t_{rec}. Because the maximum excitation of $NO_{2,gas}$ and $NO_{2,ads}$ both occur in the violet-light region for PbSe, CdSe, and CdS, the optimal spectral region for reducing t_{res} and t_{rec} is the violet region. However, dissimilarities in the electron density difference plots for $NO_{2,ads}$ on PbSe and on CdSe/S enable violet light to be more effective in shortening t_{rec} of PbSe QD gel than CdSe/S QD gels. Nevertheless, the reduced t_{rec} comes at a price of reduced charge transfer between NO_2 and the QD gel, leading to a decreased sensor response, underscoring the delicate balancing act of sensor optimization.

Negative Control Using SO_2. To further validate our proposed theory, we carried out a negative control experiment using SO_2. We chose SO_2 because (1) like NO_2, the sensing mechanism involves electron transfer from the QD to the analyte and (2) neither $SO_{2,gas}$ nor $SO_{2,ads}$ are excited by the LED lights used in our study, which span 365−625 nm. Specifically, $SO_{2,gas}$ absorbs in the UV region at a wavelength <∼340 nm (Figure 4a) and the ECW calculation results (Figure S15) reveal that excitation of $SO_{2,ads}$ on PbSe occurs at 3.65 eV (339.7 nm). Consistent with expectation, we observed no photothermal effect for SO_2 under violet-light illumination (Figure 4f). The response−recovery curves of a PbSe QD gel sensor toward 1.32 ppm SO_2 under various light conditions, as shown in Figure S16, exhibit minimal changes in response, t_{res}, and t_{rec}. For example, the response, t_{res}, and t_{rec} were decreased by merely 4.2, 4.0, and 4.6% under violet light (Table S6) relative to no-light condition results, respectively, further confirming our proposed theory.

CONCLUSIONS

In conclusion, we demonstrate accelerated response and recovery rates for NO_2 sensing on QD (PbSe, CdSe, CdS) gel platforms upon violet-light illumination, leading to one of the best performing room-temperature p-type NO_2 sensors to date. The best performing PbSe QD gel sensor is characterized by a good sensor response (0.04%/ppb), ultralow LOD (3 ppb, the lowest experimentally measured LOD), and short t_{res} and t_{rec} (27 and 102 s, among the top 10 response/recovery speeds reported in the literature). Critically, the work revealed the crucial roles of excited NO_2 gaseous molecules and adsorbed NO_2 in the light-activated gas-sensing phenomenon, directly contradicting the prevailing theory of light-activated sensing driven by photogenerated electron−hole pairs in the semiconductor sensor (i.e., achieved by tuning the illumination wavelength to the band gap of the sensor). These new findings suggest the design of high-performance light-activated gas sensors can benefit from a careful assessment of the photophysical characteristics of the analyte in the gas phase vs those adsorbed onto the specific semiconductor surface.

ASSOCIATED CONTENT

Supporting Information

The Supporting Information is available free of charge at https://pubs.acs.org/doi/10.1021/acssensors.1c01694.

https://doi.org/10.1021/acssensors.1c01694
ACS Sens. XXXX, XXX, XXX−XXX

Methods, STEM images and size distribution histogram of CdSe and CdS QDs, PXRD patterns, nitrogen adsorption and desorption isotherms, and Tauc plots of PbSe, CdSe, and CdSe QD gels, FE-SEM cross-section images of PbSe, CdSe, and CdS gel sensors, photographs of the gas sensor test apparatus, response−recovery curves of PbSe gel sensors toward NO_2 at various concentrations and under different light wavelengths, sensor response vs NO_2 concentration plots, a typical sensor response−recovery trace, the photothermal effect results under various light wavelengths, the partition of the CdS/Se-NO_2 system, oscillator strengths of PbSe- and CdSe/S-NO_2 systems, the active space of a NO_2 molecule, theoretical results on the PbSe-SO_2 system, the sensing performance of a PbSe QD gel toward SO_2 under various light wavelengths, a summary of t_{res} and t_{rec} of 202 state-of-the-art room-temperature NO_2 gas sensors, a summary of the performance of 110 state-of-the-art room-temperature p-type NO_2 gas sensors, the average crystallite sizes of PbSe, CdSe, and CdS QD gels estimated from the PXRD peak widths, BET data, comparison between NO_2 and SO_2 sensing performance of a PbSe gel sensor under violet light, and the wavelength ranges of LED lights used in the study (PDF)

AUTHOR INFORMATION

Corresponding Authors

Ting Tan − *Laboratory of Theoretical and Computational Nanoscience, CAS Center for Excellence in Nanoscience, National Center for Nanoscience and Technology, Chinese Academy of Sciences, Beijing 100190, China*; Email: tant@nanoctr.cn

Long Luo − *Department of Chemistry, Wayne State University, Detroit, Michigan 48202, United States*; orcid.org/0000-0001-5771-6892; Email: long.luo@wayne.edu

Authors

Xin Geng − *Department of Chemistry, Wayne State University, Detroit, Michigan 48202, United States*

Xiaolong Liu − *Laboratory of Theoretical and Computational Nanoscience, CAS Center for Excellence in Nanoscience, National Center for Nanoscience and Technology, Chinese Academy of Sciences, Beijing 100190, China*

Lalani Mawella-Vithanage − *Department of Chemistry, Wayne State University, Detroit, Michigan 48202, United States*

Chathuranga C. Hewa-Rahinduwage − *Department of Chemistry, Wayne State University, Detroit, Michigan 48202, United States*

Liang Zhang − *School of Vehicle and Mobility, Tsinghua University, Beijing 100084, China; Center for Combustion Energy, Tsinghua University, Beijing 100084, China*; orcid.org/0000-0002-9718-0436

Stephanie L. Brock − *Department of Chemistry, Wayne State University, Detroit, Michigan 48202, United States*; orcid.org/0000-0002-0439-302X

Complete contact information is available at: https://pubs.acs.org/10.1021/acssensors.1c01694

Author Contributions

⊥X.G. and X.L. contributed equally to this work.

Notes

The authors declare no competing financial interest.

ACKNOWLEDGMENTS

This work was financially supported by the Start-up Funds of L.L. from Wayne State University; L.M.-V. and S.L.B. additionally acknowledge support from DMR-1904775. The authors thank BW. Wang and E. Nikolla at Wayne State University for carrying out the Surface Area Analysis measurements, T. Ma at the Michigan Center from the University of Michigan for STEM characterization using a JEOL3100R05 funded by NSF grant #DMR-0723032, and Prof. Emily A Carter's group for the suggestions on ECW calculations. This work also utilizes a JEOL-2010 TEM supported by NSF grant #0216084 and the PXRD Facility supported by NSF grant #1427926.

REFERENCES

(1) Guarnieri, M.; Balmes, J. R. Outdoor air pollution and asthma. *Lancet* **2014**, *383*, 1581−1592.

(2) Alving, K.; Weitzberg, E.; Lundberg, J. Increased amount of nitric oxide in exhaled air of asthmatics. *Eur. Respir. J.* **1993**, *6*, 1368−1370.

(3) Barnes, P. J.; Dweik, R. A.; Gelb, A. F.; Gibson, P. G.; George, S. C.; Grasemann, H.; Pavord, I. D.; Ratjen, F.; Silkoff, P. E.; Taylor, D. R.; et al. Exhaled nitric oxide in pulmonary diseases: a comprehensive review. *Chest* **2010**, *138*, 682−692.

(4) Liang, D.; Shi, L.; Zhao, J.; Liu, P.; Sarnat, J. A.; Gao, S.; Schwartz, J.; Liu, Y.; Ebelt, S. T.; Scovronick, N.; Chang, H. H. Urban Air Pollution May Enhance COVID-19 Case-Fatality and Mortality Rates in the United States. *Innovation* **2020**, *1*, No. 100047.

(5) Korotcenkov, G.; Cho, B. Metal oxide composites in conductometric gas sensors: Achievements and challenges. *Sens. Actuators, B* **2017**, *244*, 182−210.

(6) Xuan, J.; Zhao, G.; Sun, M.; Jia, F.; Wang, X.; Zhou, T.; Yin, G.; Liu, B. Low-temperature operating ZnO-based NO_2 sensors: a review. *RSC Adv.* **2020**, *10*, 39786−39807.

(7) Ou, J. Z.; Ge, W.; Carey, B.; Daeneke, T.; Rotbart, A.; Shan, W.; Wang, Y.; Fu, Z.; Chrimes, A. F.; Wlodarski, W.; Russo, S. P.; Li, Y. X.; Kalantar-zadeh, K. Physisorption-Based Charge Transfer in Two-Dimensional SnS_2 for Selective and Reversible NO_2 Gas Sensing. *ACS Nano* **2015**, *9*, 10313−10323.

(8) Ko, K. Y.; Song, J.-G.; Kim, Y.; Choi, T.; Shin, S.; Lee, C. W.; Lee, K.; Koo, J.; Lee, H.; Kim, J.; Lee, T.; Park, J.; Kim, H. Improvement of Gas-Sensing Performance of Large-Area Tungsten Disulfide Nanosheets by Surface Functionalization. *ACS Nano* **2016**, *10*, 9287−9296.

(9) Anothainart, K.; Burgmair, M.; Karthigeyan, A.; Zimmer, M.; Eisele, I. Light enhanced NO_2 gas sensing with tin oxide at room temperature: conductance and work function measurements. *Sens. Actuators, B* **2003**, *93*, 580−584.

(10) Hewa-Rahinduwage, C. C.; Geng, X.; Silva, K. L.; Niu, X.; Zhang, L.; Brock, S. L.; Luo, L. Reversible Electrochemical Gelation of Metal Chalcogenide Quantum Dots. *J. Am. Chem. Soc.* **2020**, *142*, 12207−12215.

(11) Xu, F.; Ho, H.-P. Light-activated metal oxide gas sensors: A review. *Micromachines* **2017**, *8*, No. 333.

(12) Lu, G.; Xu, J.; Sun, J.; Yu, Y.; Zhang, Y.; Liu, F. UV-enhanced room temperature NO_2 sensor using ZnO nanorods modified with SnO_2 nanoparticles. *Sens. Actuators, B* **2012**, *162*, 82−88.

(13) Kumar, R.; Goel, N.; Kumar, M. UV-Activated MoS_2 Based Fast and Reversible NO_2 Sensor at Room Temperature. *ACS Sens.* **2017**, *2*, 1744−1752.

(14) Zheng, W.; Xu, Y.; Zheng, L.; Yang, C.; Pinna, N.; Liu, X.; Zhang, J. MoS_2 Van der Waals p−n Junctions Enabling Highly

Selective Room-Temperature NO_2 Sensor. *Adv. Mater. Interfaces* **2020**, *30*, No. 2000435.
(15) Late, D. J.; Huang, Y.-K.; Liu, B.; Acharya, J.; Shirodkar, S. N.; Luo, J.; Yan, A.; Charles, D.; Waghmare, U. V.; Dravid, V. P.; Rao, C. N. R. Sensing Behavior of Atomically Thin-Layered MoS_2 Transistors. *ACS Nano* **2013**, *7*, 4879−4891.
(16) Tabata, H.; Matsuyama, H.; Goto, T.; Kubo, O.; Katayama, M. Visible-Light-Activated Response Originating from Carrier-Mobility Modulation of NO_2 Gas Sensors Based on MoS_2 Monolayers. *ACS Nano* **2021**, *15*, 2542−2553.
(17) Zhou, Y.; Zou, C.; Lin, X.; Guo, Y. UV light activated NO_2 gas sensing based on Au nanoparticles decorated few-layer MoS_2 thin film at room temperature. *Appl. Phys. Lett.* **2018**, *113*, No. 082103.
(18) Wu, E.; Xie, Y.; Yuan, B.; Zhang, H.; Hu, X.; Liu, J.; Zhang, D. Ultrasensitive and Fully Reversible NO_2 Gas Sensing Based on p-Type $MoTe_2$ under Ultraviolet Illumination. *ACS Sens.* **2018**, *3*, 1719−1726.
(19) Yan, W.-J.; Chen, D.-Y.; Fuh, H.-R.; Li, Y.-L.; Zhang, D.; Liu, H.; Wu, G.; Zhang, L.; Ren, X.; Cho, J.; Choi, M.; Chun, B. S.; Coileáin, C. Ó.; Xu, H.-J.; Wang, Z.; Jiang, Z.; Chang, C.-R.; Wu, H.-C. Photo-enhanced gas sensing of SnS_2 with nanoscale defects. *RSC Adv.* **2019**, *9*, 626−635.
(20) Gu, D.; Wang, X.; Liu, W.; Li, X.; Lin, S.; Wang, J.; Rumyantseva, M. N.; Gaskov, A. M.; Akbar, S. A. Visible-light activated room temperature NO_2 sensing of SnS_2 nanosheets based chemiresistive sensors. *Sens. Actuators, B* **2020**, *305*, No. 127455.
(21) Yan, X.; Wu, Y.; Li, R.; Shi, C.; Moro, R.; Ma, Y.; Ma, L. High-Performance UV-Assisted NO_2 Sensor Based on Chemical Vapor Deposition Graphene at Room Temperature. *ACS Omega* **2019**, *4*, 14179−14187.
(22) Jo, Y.-M.; Lim, K.; Yoon, J. W.; Jo, Y. K.; Moon, Y. K.; Jang, H. W.; Lee, J.-H. Visible-Light-Activated Type II Heterojunction in Cu_3(hexahydroxytriphenylene)$_2$/Fe_2O_3 Hybrids for Reversible NO_2 Sensing: Critical Role of $\pi-\pi^*$ Transition. *ACS Cent. Sci.* **2021**, *7*, 1176−1182.
(23) Pham, T.; Li, G.; Bekyarova, E.; Itkis, M. E.; Mulchandani, A. MoS_2-based optoelectronic gas sensor with sub-parts-per-billion limit of NO_2 gas detection. *ACS Nano* **2019**, *13*, 3196−3205.
(24) Zhang, L.; Li, Z.; Liu, J.; Peng, Z.; Zhou, J.; Zhang, H.; Li, Y. Optoelectronic Gas Sensor Based on Few-Layered InSe Nanosheets for NO_2 Detection with Ultrahigh Antihumidity Ability. *Anal. Chem.* **2020**, *92*, 11277−11287.
(25) Liu, B.; Luo, Y.; Li, K.; Wang, H.; Gao, L.; Duan, G. Room-temperature NO_2 gas sensing with ultra-sensitivity activated by ultraviolet light based on SnO_2 monolayer array film. *Adv. Mater. Interfaces* **2019**, *6*, No. 1900376.
(26) Klüner, T.; Govind, N.; Wang, Y. A.; Carter, E. A. Periodic density functional embedding theory for complete active space self-consistent field and configuration interaction calculations: Ground and excited states. *J. Chem. Phys.* **2002**, *116*, 42−54.
(27) Huang, P.; Carter, E. A. Local electronic structure around a single Kondo impurity. *Nano Lett.* **2006**, *6*, 1146−1150.
(28) Zhao, Q.; Zhang, X.; Martirez, J. M. P.; Carter, E. A. Benchmarking an embedded adaptive sampling configuration interaction method for surface reactions: H_2 desorption from and CH_4 dissociation on Cu (111). *J. Chem. Theory Comput.* **2020**, *16*, 7078−7088.
(29) Bao, J. L.; Carter, E. A. Surface-plasmon-induced ammonia decomposition on copper: Excited-state reaction pathways revealed by embedded correlated wavefunction theory. *ACS Nano* **2019**, *13*, 9944−9957.
(30) Zhou, L.; Martirez, J. M. P.; Finzel, J.; Zhang, C.; Swearer, D. F.; Tian, S.; Robatjazi, H.; Lou, M.; Dong, L.; Henderson, L.; et al. Light-driven methane dry reforming with single atomic site antenna-reactor plasmonic photocatalysts. *Nat. Energy* **2020**, *5*, 61−70.
(31) Davis, J. L.; Chalifoux, A. M.; Brock, S. L. Role of Crystal Structure and Chalcogenide Redox Properties on the Oxidative Assembly of Cadmium Chalcogenide Nanocrystals. *Langmuir* **2017**, *33*, 9434−9443.
(32) Silva, K. L.; Silmi, L.; Brock, S. L. Effect of metal ion solubility on the oxidative assembly of metal sulfide quantum dots. *J. Chem. Phys.* **2019**, *151*, No. 234715.
(33) Pala, I. R.; Brock, S. L. ZnS nanoparticle gels for remediation of Pb^{2+} and Hg^{2+} polluted water. *ACS Appl. Mater. Interfaces* **2012**, *4*, 2160−2167.
(34) Yu, H.; Liu, Y.; Brock, S. L. Tuning the optical band gap of quantum dot assemblies by varying network density. *ACS Nano* **2009**, *3*, 2000−2006.
(35) Borchert, H.; Shevchenko, E. V.; Robert, A.; Mekis, I.; Kornowski, A.; Grübel, G.; Weller, H. Determination of nanocrystal sizes: a comparison of TEM, SAXS, and XRD studies of highly monodisperse $CoPt_3$ particles. *Langmuir* **2005**, *21*, 1931−1936.
(36) Gelb, L. D.; Gubbins, K. Characterization of porous glasses: Simulation models, adsorption isotherms, and the Brunauer−Emmett−Teller analysis method. *Langmuir* **1998**, *14*, 2097−2111.
(37) Barrett, E. P.; Joyner, L. G.; Halenda, P. P. The Determination of Pore Volume and Area Distributions in Porous Substances. I. Computations from Nitrogen Isotherms. *J. Am. Chem. Soc.* **1951**, *73*, 373−380.
(38) Ou, G.; Li, D.; Pan, W.; Zhang, Q.; Xu, B.; Gu, L.; Nan, C.; Wu, H. Arc-melting to narrow the bandgap of oxide semiconductors. *Adv. Mater.* **2015**, *27*, 2589−2594.
(39) Khan, Z.; Khannam, M.; Vinothkumar, N.; De, M.; Qureshi, M. Hierarchical 3D NiO−CdS heteroarchitecture for efficient visible light photocatalytic hydrogen generation. *J. Mater. Chem.* **2012**, *22*, 12090−12095.
(40) Aminorroaya Yamini, S.; Patterson, V.; Santos, R. Band-gap nonlinearity in lead chalcogenide (PbQ, Q= Te, Se, S) alloys. *ACS Omega* **2017**, *2*, 3417−3423.
(41) Rajeshwar, K.; de Tacconi, N. R.; Chenthamarakshan, C. Semiconductor-based composite materials: preparation, properties, and performance. *Chem. Mater.* **2001**, *13*, 2765−2782.
(42) Jie, J. S.; Zhang, W. J.; Jiang, Y.; Meng, X. M.; Li, Y. Q.; Lee, S. T. Photoconductive Characteristics of Single-Crystal CdS Nanoribbons. *Nano Lett.* **2006**, *6*, 1887−1892.
(43) Amalnerkar, D. P. Photoconducting and allied properties of CdS thick films. *Mater. Chem. Phys.* **1999**, *60*, 1−21.
(44) Zhang, C.; Wang, J.; Olivier, M.-G.; Debliquy, M. Room temperature nitrogen dioxide sensors based on N719-dye sensitized amorphous zinc oxide sensors performed under visible-light illumination. *Sens. Actuators, B* **2015**, *209*, 69−77.
(45) Zhang, C.; Boudiba, A.; De Marco, P.; Snyders, R.; Olivier, M.-G.; Debliquy, M. Room temperature responses of visible-light illuminated WO_3 sensors to NO_2 in sub-ppm range. *Sens. Actuators, B* **2013**, *181*, 395−401.
(46) Eom, T. H.; Cho, S. H.; Suh, J. M.; Kim, T.; Lee, T. H.; Jun, S. E.; Yang, J. W.; Lee, J.; Hong, S.-H.; Jang, H. W. Substantially improved room temperature NO_2 sensing in 2-dimensional SnS_2 nanoflowers enabled by visible light illumination. *J. Mater. Chem. A* **2021**, *9*, 11168−11178.
(47) Li, H.-Y.; Yoon, J.-W.; Lee, C.-S.; Lim, K.; Yoon, J.-W.; Lee, J.-H. Visible light assisted NO_2 sensing at room temperature by CdS nanoflake array. *Sens. Actuators, B* **2018**, *255*, 2963−2970.
(48) Krzempek, K. A review of photothermal detection techniques for gas sensing applications. *Appl. Sci.* **2019**, *9*, No. 2826.
(49) Li, S.; Matthews, J.; Sinha, A. Atmospheric Hydroxyl Radical Production from Electronically Excited NO_2 and H_2O. *Science* **2008**, *319*, 1657−1660.
(50) Andersson, K.; Malmqvist, P. Å.; Roos, B. O. Second-order perturbation theory with a complete active space self-consistent field reference function. *J. Chem. Phys.* **1992**, *96*, 1218−1226.

https://doi.org/10.1021/acssensors.1c01694
ACS Sens. XXXX, XXX, XXX−XXX